

Provided for non-commercial research and education use.  
Not for reproduction, distribution or commercial use.



This article appeared in a journal published by Elsevier. The attached copy is furnished to the author for internal non-commercial research and education use, including for instruction at the authors institution and sharing with colleagues.

Other uses, including reproduction and distribution, or selling or licensing copies, or posting to personal, institutional or third party websites are prohibited.

In most cases authors are permitted to post their version of the article (e.g. in Word or Tex form) to their personal website or institutional repository. Authors requiring further information regarding Elsevier's archiving and manuscript policies are encouraged to visit:

<http://www.elsevier.com/authorsrights>



Contents lists available at ScienceDirect

## Earth and Planetary Science Letters

[www.elsevier.com/locate/epsl](http://www.elsevier.com/locate/epsl)

# Integration of Chang'E-2 imagery and LRO laser altimeter data with a combined block adjustment for precision lunar topographic modeling

Bo Wu <sup>a</sup>, Han Hu <sup>a,b,c,\*</sup>, Jian Guo <sup>a</sup><sup>a</sup> Department of Land Surveying and Geo-Informatics, The Hong Kong Polytechnic University, Hung Hom, Kowloon, Hong Kong<sup>b</sup> State Key Laboratory of Information Engineering in Surveying Mapping and Remote Sensing, Wuhan University, Wuhan, PR China<sup>c</sup> Faculty of Geosciences and Environmental Engineering, Southwest Jiaotong University, Chengdu, PR China

## ARTICLE INFO

## Article history:

Received 10 June 2013

Received in revised form 16 December 2013

Accepted 14 January 2014

Available online 6 February 2014

Editor: C. Sotin

## Keywords:

lunar topography

Chang'E-2 imagery

LRO LOLA

cross-mission data integration

block adjustment

## ABSTRACT

Lunar topographic information is essential for lunar scientific investigations and exploration missions. Lunar orbiter imagery and laser altimeter data are two major data sources for lunar topographic modeling. Most previous studies have processed the imagery and laser altimeter data separately for lunar topographic modeling, and there are usually inconsistencies between the derived lunar topographic models. This paper presents a novel combined block adjustment approach to integrate multiple strips of the Chinese Chang'E-2 imagery and NASA's Lunar Reconnaissance Orbiter (LRO) Laser Altimeter (LOLA) data for precision lunar topographic modeling. The participants of the combined block adjustment include the orientation parameters of the Chang'E-2 images, the intra-strip tie points derived from the Chang'E-2 stereo images of the same orbit, the inter-strip tie points derived from the overlapping area of two neighbor Chang'E-2 image strips, and the LOLA points. Two constraints are incorporated into the combined block adjustment including a local surface constraint and an orbit height constraint, which are specifically designed to remedy the large inconsistencies between the Chang'E-2 and LOLA data sets. The output of the combined block adjustment is the improved orientation parameters of the Chang'E-2 images and ground coordinates of the LOLA points, from which precision lunar topographic models can be generated. The performance of the developed approach was evaluated using the Chang'E-2 imagery and LOLA data in the Sinus Iridum area and the Apollo 15 landing area. The experimental results revealed that the mean absolute image residuals between the Chang'E-2 image strips were drastically reduced from tens of pixels before the adjustment to sub-pixel level after adjustment. Digital elevation models (DEMs) with 20 m resolution were generated using the Chang'E-2 imagery after the combined block adjustment. Comparison of the Chang'E-2 DEM with the LOLA DEM showed a good level of consistency. The developed combined block adjustment approach is of significance for the full comparative and synergistic use of lunar topographic data sets from different sensors and different missions.

© 2014 Elsevier B.V. All rights reserved.

## 1. Introduction

Lunar topography is one of the principal measurements that quantitatively describe the body of the Moon. Together with gravity data, it enables the mapping of subsurface density anomalies and yields information on not only the shape but also the internal structure of the Moon (Smith et al., 1997). Such information is critical to understanding the structure of the Moon's crust, which has major implications for the thermal history of the Moon (Garvin et al., 1999; Wieczorek et al., 2006). High resolution and precision lunar topographic data also play critical roles in lunar exploration missions, in such areas as the selection of landing sites, the safe

maneuvering of lunar vehicles or robots, and the navigation of astronauts in ground operations (Wu et al., 2013).

Lunar orbiter imagery and laser altimeter data are two major data sources for lunar topographic modeling. Recent lunar exploration missions, such as the Chinese Chang'E-1 (launched in October 2007) and the Chang'E-2 (launched in October 2010) (Ouyang et al., 2010), the Japanese SELENological and ENgineering Explorer (SELENE)/Kaguya (launched in September 2007) (Kato et al., 2008), India's Chandrayaan-1 (launched in October 2008) (Vighnesham et al., 2010), and NASA's Lunar Reconnaissance Orbiter (LRO) (launched in June 2009) (Vondrak et al., 2010), have involved the use of orbiter cameras and laser altimeters with different configurations on-board the spacecraft. They have collected vast amounts of lunar topographic data at different resolutions and levels of uncertainty. Most previous related research has processed the orbiter imagery and laser altimeter data for lunar topographic modeling separately (Araki et al., 2009; Li et al., 2010a, 2010b;

\* Corresponding author at: State Key Laboratory of Information Engineering in Surveying Mapping and Remote Sensing, Wuhan University, Wuhan, PR China.

E-mail address: [huhan@whu.edu.cn](mailto:huhan@whu.edu.cn) (H. Hu).

Mazarico et al., 2011; Di et al., 2012; Haruyama et al., 2012; Scholten et al., 2012; Robinson et al., 2012), and there are usually inconsistencies between the derived lunar topographic models (e.g. digital elevation models (DEMs)). The correlation or integration of cross-sensor data (e.g. lunar imagery and laser altimeter data) has the potential to produce consistent and precise topographic models, which cannot be achieved when only using the data from a single type of sensor (Rosiek et al., 2001; Wu et al., 2011a; Di et al., 2012). Wu et al. (2011a) proposed the integration of the Chang'E-1 imagery and laser altimeter data for lunar topographic modeling through a least-squares adjustment approach, in which the Chang'E-1 laser altimeter points, the orientation parameters of the Chang'E-1 images, and tie points collected from the stereo Chang'E-1 images are processed and adjusted to export the refined image orientation parameters and laser ground points. This approach eliminates the inconsistencies between the imagery and laser altimeter data and allows the generation of precision lunar topographic models. However, the approach was designed for the integration of Chang'E-1 imagery and Chang'E-1 laser altimeter data. The inconsistencies between these two data sets are moderate because they were collected by sensors onboard the same spacecraft Chang'E-1 (Wu et al., 2011a). In addition, the approach was designed for single strip image processing and did not consider multi-strip images for lunar topographic modeling within large image blocks. Lunar topographic modeling using multi-strip images requires block adjustment (Brown, 1976; Cramer and Haala, 2010) of the images, so that the inconsistencies in the inter-strip overlapping areas can be eliminated.

This paper aims at cross-mission and cross-sensor data integration for precision lunar topographic modeling. The existing approach (Wu et al., 2011a) will be improved and extended to integrate data from Chang'E-2 imagery and the Lunar Reconnaissance Orbiter (LRO) Laser Altimeter (LOLA). Integration of cross-mission lunar imagery and laser altimeter data is a more challenging task because the effect of uncertainties between the data sets collected by different sensors from different missions is more significant. For example, DEMs were derived from the Chang'E-2 imagery (Zou et al., 2012) and LOLA data separately in relation to the Sinus Iridum area on the Moon. The statistics of the elevation differences between these two types of DEM have shown that the Chang'E-2 data is about 300 m lower than the LOLA data on average. Nevertheless, this cross-mission and cross-sensor data integration strategy is very valuable for the integration of data sets from different sources to generate consistent and precise lunar topographic models, which will permit the full comparative and synergistic use of such data sets. This paper presents a novel combined block adjustment approach for the integration of Chang'E-2 imagery and LOLA data covering large areas with multi-strip images. The combined block adjustment of Chang'E-2 imagery and LOLA data can enhance the geometric consistency between multi-strip Chang'E-2 images and between the Chang'E-2 imagery and LOLA data, so that the accuracy of topographic modeling in large block areas can be further improved.

After presenting a literature review on lunar topographic modeling from various lunar orbital imagery and laser altimeter data, this paper describes the specifications of Chang'E-2 imagery and LOLA data. The combined block adjustment approach for the integration of Chang'E-2 imagery and LOLA data is then presented in detail. The Chang'E-2 imagery and LOLA data for the Sinus Iridum area ( $18^{\circ}$  to  $25.7^{\circ}$  W and  $42^{\circ}$  to  $46.3^{\circ}$  N) and the Apollo 15 landing area ( $0.15^{\circ}$  to  $4^{\circ}$  E and  $24^{\circ}$  to  $28^{\circ}$  N) are used for experimental analysis. The performance of the proposed method is then evaluated. Finally, concluding remarks are given.

## 2. Related work

Lunar exploration missions in recent years have collected a vast amount of lunar surface images and elevation measurements through the use of cameras and laser altimeters onboard the spacecraft. The CCD camera onboard the Chinese Chang'E-1 spacecraft returned 1098 orbiter images with a spatial resolution of 120 m. A global DEM was produced using these images. The grid size for this DEM is up to 500 m and the planar positioning accuracy is about 370 m (Liu et al., 2009). A global topographic map of the Moon at a scale of 1:2,500,000 was also produced using the Chang'E-1 imagery; its planar positioning accuracy ranges from 100 m to 1.5 km (Li et al., 2010a). The laser altimeter onboard the Chang'E-1 spacecraft collected more than nine million range measurements covering the entire Moon. The measurements had spacing resolutions of 1.4 km for the along-track direction and 7 km for the cross-track direction (at the equator), from which a global DEM with 3-km grid spacing was produced. The plane positioning accuracy of the DEM was 445 m, and the vertical accuracy was 60 m (Li et al., 2010b).

The Japanese SELENE mission also collected stereoscopic images with a spatial resolution of 10 m using its push-broom Terrain Camera, which covered almost the entire surface of the Moon. A global DEM mosaic with 10-m spatial resolution was produced from this camera imagery. The locations of the Apollo Laser Ranging RetroReflector (LRRR) were compared with this DEM. The results revealed differences ranging from  $-17$  m to 5 m for longitude, from  $-20$  m to 48 m for latitude, and from 3 to 5 m for elevation (Haruyama et al., 2012). The SELENE laser altimeter collected more than 10 million high-quality range measurements covering the entire lunar surface with a height resolution of 5 m at a sampling interval smaller than 2 km (Araki et al., 2009). A global lunar topographic map with a spatial resolution of 0.5 degree was derived from the SELENE laser altimeter data (Araki et al., 2009).

India's Chandrayaan-1 was equipped with a Terrain Mapping Camera with an imaging capability of 5-m spatial resolution. The collected images partially covered the lunar surface and were used to produce regional DEMs (Arya et al., 2011; Radhadevi et al., 2013). The root mean square (RMS) error of the DEMs was about 200–300 m in latitude, longitude, and height with respect to the references of Clementine base map mosaic and LOLA data (Radhadevi et al., 2013). The laser altimeter onboard Chandrayaan-1 was able to provide range measurements with range resolution better than 5 m (Kamalakar et al., 2009). The collected laser altimeter data cover both of the lunar poles and other lunar regions of interest.

There are two cameras onboard the LRO spacecraft: a wide-angle camera (WAC) and the narrow-angle camera (NAC). The cameras have collected lunar images with spatial resolutions of 100 m and 50 cm, respectively. The WAC images provide global coverage, and a near-global DEM GLD100 with grid spacing of 100 m was produced from them (Scholten et al., 2012). The NAC images cover only a small portion of the lunar surface, but that includes complete coverage of both poles (Robinson et al., 2012). Regional DEMs with meter-level resolution have been generated from the NAC images (Tran et al., 2010; Burns et al., 2012). The LOLA onboard the LRO measures the distance to the lunar surface at five spots simultaneously (Smith et al., 2010). The five-spot pattern provides five adjacent profiles for each track. The spacing resolution in the along-track direction is 10 to 12 m within the combined measurements in the five adjacent profiles. The average distance between LOLA tracks is in the order of 1–2 km at the equator and decreases at higher latitudes. LOLA measurements are generally very dense (varying from a few meters to tens of meters) at polar sites. LOLA Digital Elevation Models (LDEM) are built by binning all valid measurements into the map grid cells and are generated at multiple

resolutions. The LDEM\_1024 from the LOLA release 8 in the Planetary Data System (PDS) has the best resolution of 1024 PPD (pixel per degree), which is equivalent to about 30 m/pixel in latitude. However, it should be noted that not every pixel in the LDEM\_1024 has a measurement, depending on the latitudes of the locations.

As described above, most previous research has processed the lunar imagery and laser altimeter data separately. Research reports have occasionally emphasized cross-sensor and cross-mission data integration for lunar topographic modeling. The Unified Lunar Control Network (ULCN), which dated back to Brown (1968), had combined the earth-based LRRR (Lunar Laser Ranging Retroreflector) measurements and telescopic observations to form a network of lunar ground control points. Light (1972) and Doyle et al. (1976) were among the first to integrate observations of synchronized instruments on board the same spacecraft to create lunar topographic models using the data collected from Apollo missions 15, 16, and 17. Light (1972) adopted the distance measurements from a laser altimeter to constrain the orbiter height of the optical camera. Doyle et al. (1976) employed the stellar camera to help orient the optical camera with preflight calibrated lock-angles, and used the laser altimeter observations to help determine the scale of the stereo model of the images collected by the optical camera. Rosiek et al. (2001) attempted to combine the Clementine images with the Clementine laser altimeter data. The images were used to establish horizontal control and the laser altimeter data were used for vertical control. However, the two data sets did not align well with each other due to the marginal overlap between the stereo models. Radhadevi et al. (2013) presented a geometric correction method for Chandrayaan-1 imagery. The planimetric control was identified from the Clementine base map mosaic and vertical control was derived from LOLA data. This method only used the Clementine and LOLA data as control information in the photogrammetric processing of Chandrayaan-1 imagery, and the control information was very limited. Di et al. (2012) studied the co-registration of Chang'E-1 stereo images and laser altimeter data. A crossover adjustment was first used to remove the crossover differences between the different laser altimeter tracks. An ICP (iterative closest point) algorithm was used to register the 3D points derived from the stereo images to the laser altimeter points, from which the image orientation parameters were refined so that the images and laser altimeter data were co-registered. However, this method treated the Chang'E-1 laser altimeter data as the absolute control and the accuracy of the final generated topographic models was totally dependent on the accuracy of the laser altimeter data.

Integration of multi-source remote sensing imagery and laser altimeter data has been used for topographic mapping of Earth and Mars. An early example of using additional data sources (e.g. DEM) as control information for aerial triangulation was the approach presented by Ebner et al. (1991). This approach focused mainly on the satisfaction of accuracy for middle- and small-scale photogrammetry for Earth aerial and satellite image processing by minimizing the differences between the heights derived from stereo images and using the interpolated heights from a DEM as constraints. Jaw (2000) proposed a method in which additional surface information was integrated into the aerial triangulation workflow by hypothesizing plane observations in the object space. The estimated object points derived from image measurements together with the adjusted surface points provided a better point group describing the surface. Teo et al. (2010) investigated the block adjustment of three SPOT 5 images using a DEM as the elevation control. Common tie points were first identified from images. Initial ground coordinates of the points were derived from space intersection using the image orientation parameters. The elevation coordinates of the points were then interpolated from the DEM based on their planimetric coordinates, and their ground coordinates were further adjusted through an iteration procedure in

the block adjustment. The experimental results indicated that using the DEM as an elevation control can improve geometric accuracy and reduce geometric discrepancies between images. For Mars topographic mapping applications, Anderson and Parker (2002) investigated the registration between the imagery and laser altimeter data collected by the Mars orbiter camera (MOC) and Mars orbiter laser altimeter (MOLA), both onboard the Mars Global Surveyor (MGS). Yoon and Shan (2005) presented a combined adjustment method to process the single-strip MOC imagery and MOLA data and reported that the large mis-registration between the two datasets could be reduced to a certain extent. Spiegel (2007) presented a method for the co-registration of High Resolution Stereo Camera (HRSC) images and MOLA data. A sparse stereo point cloud generated from the HRSC images was adjusted to optimize its fit to a surface interpolated from the MOLA data, from which the interior and exterior orientation parameters of the HRSC images were improved. Albertz et al. (2005) presented a method for the photogrammetric processing of HRSC imagery. The processing comprises improvements of the image EO parameters and the enhancement of the DEM quality with the assist of MOLA DEM. Gwinner et al. (2009) also produced high quality DEM products from the HRSC imagery and MOLA DEM. The proposed system had successfully created DEM of 50 m grid from stereo imagery with the ground resolution of 12 m/pixel. The differences between the DEM produced by the proposed system and that of MOLA DEM ranged from 30 to 40 m.

Compared with previous research works, the combined block adjustment approach for the integration of Chang'E-2 imagery and LOLA data presented in this paper highlights the following three aspects: (1) Cross-mission and cross-sensor lunar imagery and laser altimeter data integration has the capability of processing multi-strip images; (2) LOLA data is used as a local surface constraint to reduce the inconsistencies between the Chang'E-2 imagery and LOLA data; (3) a novel orbit height constraint is incorporated to obtain more robust and convergent results, which is crucial for the block adjustment of multi-strip images.

### 3. Specifications of Chang'E-2 imagery and LRO laser altimeter data

#### 3.1. Chang'E-2 imagery

Chang'E-2 is a Chinese lunar probe launched on October 1, 2010. It was a follow-up to the Chang'E-1 lunar probe, which was launched in 2007. Chang'E-2 was part of the first phase of the Chinese Lunar Exploration Program (Ouyang et al., 2010). The mission collected a tremendous amount of data with its various onboard payloads for lunar scientific research and in preparation for a soft landing by the Chang'E-3 lander and rover (Wang et al., 2012). Chang'E-2 completed its lunar exploration mission on June 8, 2011. It was then sent to the L2 Lagrangian point where it arrived on August 30, 2011. Chang'E-2 remained at L2 for several months and departed from L2 to the asteroid 4179 Toutatis on April 15, 2012. Chang'E-2 successfully flew by the Toutatis on December 13, 2012 and took close-up images of the asteroid. Chang'E-2 is now 20 million km away from Earth and is flying into deeper space.

Chang'E-2 used its onboard CCD camera to collect surface imagery of the Moon. Chang'E-2 flew at two types of orbit altitude. The first was a  $100 \times 100$  km circular orbit at which the CCD camera could image the lunar surface at a resolution of 7 m. The second was a  $100 \times 15$  km elliptical orbit at which the CCD camera provided imaging resolution better than 1.5 m (Zhao et al., 2011). The images collected during the first type of orbit provided global image coverage of the Moon. The higher resolution images collected during the second type of orbit provided more detailed

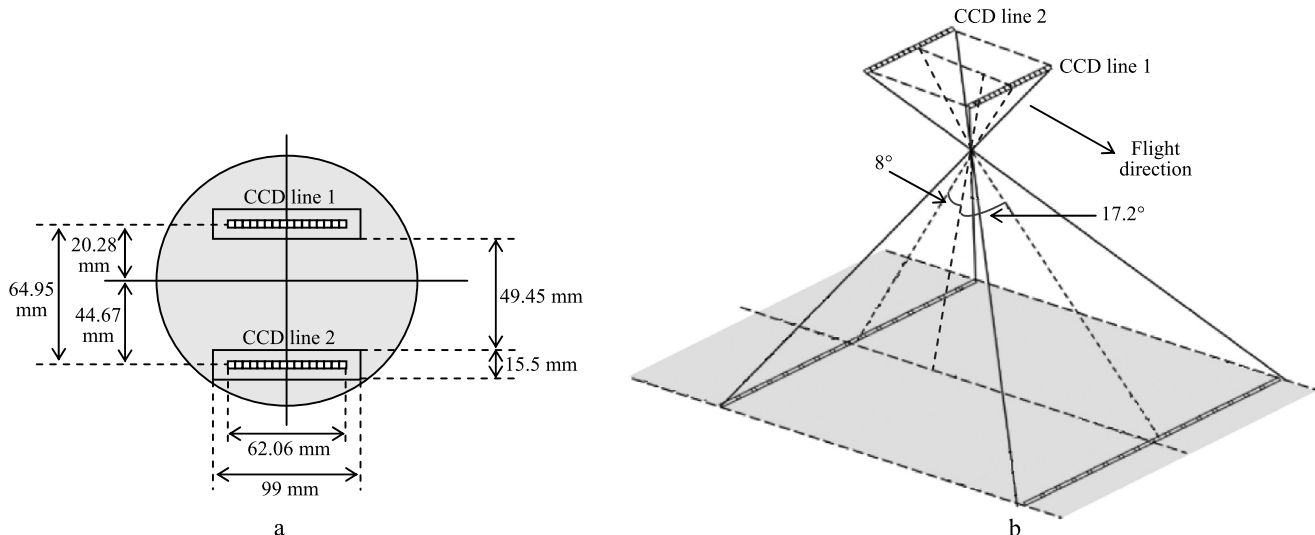


**Fig. 1.** Schematic configuration of the Chang'E-2 CCD camera. (a) Focal plane of the Chang'E-2 CCD camera and (b) stereo imaging geometry of the Chang'E-2 CCD camera.

information and were mainly used for the preparation of Chang'E-3 lunar landing mission and surface operations (Zhao et al., 2011).

The CCD camera onboard Chang'E-2 spacecraft is a two-line push-broom sensor. The two CCD lines are assembled on a unique focal plane separately, which enables the acquisition of forward- and backward-looking imagery along the flight direction simultaneously to create stereo pairs. The forward-looking imagery has a viewing angle of 8° and the backward-looking imagery has a viewing angle of 17.2°. The forward-looking CCD line is closer to the center of the focal plane and offers better imaging quality. Each CCD line is 62.06 mm in length and has 6144 pixels (pixel size: 10.1  $\mu\text{m}$ ). They share the same optical axis. The field-of-view of the camera is 42°. The schematic configuration of the Chang'E-2 CCD camera (Zhao et al., 2011) is illustrated in Fig. 1.

To model the geometry of the Chang'E-2 imagery, it is necessary to determine the coordinate frames and the IO (interior orientation) and EO (exterior orientation) parameters of the imagery. A lunar body-fixed frame is the reference frame on which the relative position and orientation of the Chang'E-2 spacecraft frame is defined. A camera frame is defined at the center of the camera focal plane, and its orientation with respect to the Chang'E-2 spacecraft frame is known. IO parameters define the intrinsic setting of the camera system. The Chang'E-2 camera optical system has a focal length of 144.3 mm. The dimensions of the CCD lines and their positions with respect to the camera focal plane are provided in Fig. 1(a). In the raw Chang'E-2 image, the row position of each pixel is related to the Ephemeris Time. The physical position of each pixel in the image with respect to the camera frame can be calculated from the IO parameters. The EO parameters define the positions of the camera's perspective center and pointing angles at a specific time. The EO parameters of each image line are different and can be retrieved by interpolating the spacecraft's trajectory and pointing vectors based on the observation time. Based on the well-known co-linearity equation (Wang, 1990), the 3D coordinates of a ground point in the lunar body-fixed coordinate system can be calculated by photogrammetric space intersection from the image coordinates of conjugate points in stereo images.

### 3.2. LRO LOLA data

The LOLA onboard the LRO is a five-spot X-pattern pulse detection altimeter, which is designed to measure the shape of the Moon by measuring precisely the range from the spacecraft to the lunar surface. LOLA operates at 28 Hz and is able to measure the

distance to lunar surface at five spots simultaneously with a nominal ranging accuracy of 10 cm (Smith et al., 2010). The five-spot pattern provides five adjacent profiles for each track, 10 m to 12 m apart over a 50- to 60-m swath, with combined measurements in the along-track direction every 10 to 12 m. This five-spot pattern of ranging measurements is very useful in the determination of surface roughness and surface slopes in local regions.

The accuracy of the topographic measurements and models derived from LOLA ranging data is very high. As reported by Mazarico et al. (2011), LOLA measurements have a precision about 10 m in the along-track and cross-track directions and 1.5 m in the radial direction, respectively, which are estimated as the root-mean-square deviation of the LRO orbit solutions, after cross-over analysis and depending on the orbit solution (Mazarico et al., 2011). The absolute accuracy of the orbit solutions, and therefore the error of the true position of the terrain point, is estimated to be of the same order of magnitude.

The LOLA data set is considered to be the most accurate topographic data set of the Moon to date. It provides much denser range measurements compared with other similar instruments from other missions.

## 4. Combined block adjustment of Chang'E-2 imagery and LRO laser altimeter data

### 4.1. Overview of the approach

A combined block adjustment model is developed for the integration of Chang'E-2 imagery and LOLA data. Since there are no tracking data or kernel data provided for the Chang'E-2 imagery used in this research, several (10–20 in general) LOLA points were manually selected on both the Chang'E-2 forward- and backward-looking images as ground control points, from which an initial set of EO parameters for the Chang'E-2 images could be derived using the method presented by King et al. (2009). The initial EO parameters were then improved through a bundle adjustment of the single-strip Chang'E-2 imagery and LOLA data using the approach presented by Wu et al. (2011a). The obtained EO parameters for each single-strip Chang'E-2 imagery were then used as input in this combined block adjustment. The combined block adjustment uses two types of tie points: intra-strip tie points and inter-strip tie points. The intra-strip tie points are the corresponding points (conjugate points representing the same textural feature) identified from the stereo images (forward- and backward-looking images)

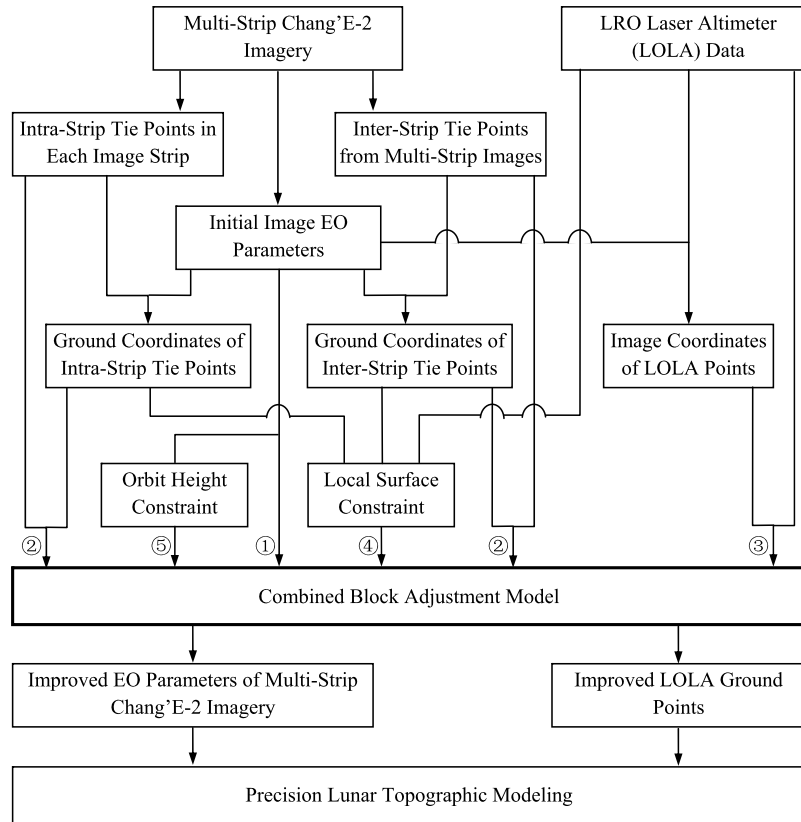


**Fig. 2.** Framework of the combined block adjustment of Chang'E-2 multi-strip imagery and LOLA data for precision lunar topographic modeling.

of the same image strip. The inter-strip tie points are the corresponding points identified from the overlapping area in the stereo images of two neighbor image strips. These tie points should be distributed evenly in the image area. Based on the IO and EO parameters of the images, the 3D coordinates of intra-strip and inter-strip tie points in the lunar body-fixed frame can be calculated from the photogrammetric space intersection. However, the image EO parameters would probably not be precise enough, and the 3D coordinates of the tie points may deviate from their true locations. There might be inconsistencies between the 3D coordinates of the same pair of inter-strip tie points identified from two neighbor image strips. In addition, based on the image orientation parameters, the LOLA ground points can be back-projected to the Chang'E-2 stereo images. If the image EO parameters are precise enough, these back-project points on the Chang'E-2 stereo images should be conjugate points representing the same textural feature. However, this is not the case due to the possible errors in the image EO parameters.

The above mentioned errors or inconsistencies can be reduced or eliminated through the combined block adjustment of the Chang'E-2 imagery and LOLA data. The participants of the combined block adjustment include the image EO parameters, the intra-strip tie points, the inter-strip tie points, the ground coordinates of the tie points, the LOLA ground points, and the back-projected image coordinates of LOLA ground points. Two additional constraints are incorporated in the block adjustment. The first is a local surface constraint, which indicates that the calculated ground coordinates of the tie points should lie in a local surface determined by its neighbor LOLA ground points. The second is an orbit height constraint, which is based on a constant circular orbit height of the Chang'E-2 spacecraft. The final output of the combined block adjustment is the improved image EO parameters and improved ground coordinates of the LOLA points. Dense image matching (Wu et al., 2011b, 2012) can then be carried out

between the stereo image pair for each image strip to generate enormous evenly distributed matched points. The 3D coordinates of the matched points can be calculated from the photogrammetric space intersection based on the improved image EO parameters, so that lunar topographic models (e.g., DEMs) with improved inter-strip consistency and improved precision can be generated. The framework of the combined block adjustment approach is shown in Fig. 2. The numbers marked in Fig. 2 correspond to the observation equations of the block adjustment model which are described in detail in the following section.

#### 4.2. Combined block adjustment model

For the Chang'E-2 stereo images, the relationship of a 3D ground point ( $X_p, Y_p, Z_p$ ) and its corresponding pixel ( $x_p, y_p$ ) can be represented by the following co-linearity equation (Wang, 1990):

$$\begin{aligned} x_p = & -f \frac{m_{11}(X_p - X_S) + m_{12}(Y_p - Y_S) + m_{13}(Z_p - Z_S)}{m_{31}(X_p - X_S) + m_{32}(Y_p - Y_S) + m_{33}(Z_p - Z_S)} \\ y_p = & -f \frac{m_{21}(X_p - X_S) + m_{22}(Y_p - Y_S) + m_{23}(Z_p - Z_S)}{m_{31}(X_p - X_S) + m_{32}(Y_p - Y_S) + m_{33}(Z_p - Z_S)} \end{aligned} \quad (1)$$

where  $(X_S, Y_S, Z_S)$  are the coordinates of the camera center in object space,  $f$  is the focal length, and  $m_{ij}$  are the elements of a rotation matrix that is determined entirely by three rotation angles ( $\varphi, \omega, \kappa$ ). The variables  $(X_S, Y_S, Z_S, \varphi, \omega, \kappa)$  are the EO parameters of the images. The EO parameters of each line in the Chang'E-2 imagery are different and can be retrieved by a polynomial function by interpolating the spacecraft's trajectory and pointing vectors based on the observation time. Several interpolation approaches have been attempted in this research to model the changes of image EO parameters including the Lagrange polynomial function, second-order polynomial, and third-order polynomial functions.

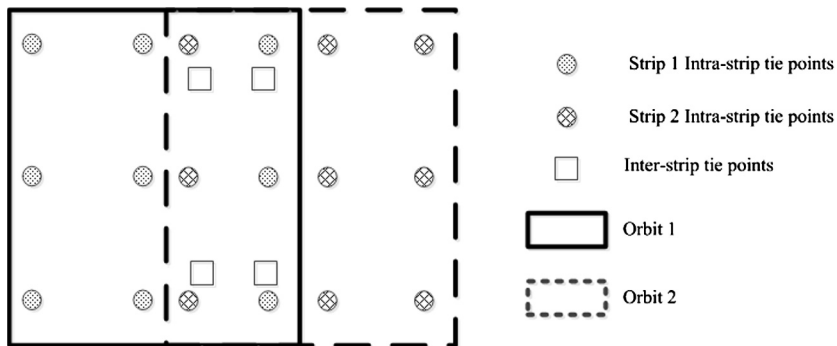


**Fig. 3.** Distribution pattern of intra- and inter-strip tie points.

The third-order polynomial function has proven to be the best and has been used in this research. The third-order polynomial function is listed as follows:

$$\begin{aligned} X_s(r) &= a_0 + a_1r + a_2r^2 + a_3r^3 \\ Y_s(r) &= b_0 + b_1r + b_2r^2 + b_3r^3 \\ Z_s(r) &= c_0 + c_1r + c_2r^2 + c_3r^3 \\ \varphi(r) &= d_0 + d_1r + d_2r^2 + d_3r^3 \\ \omega(r) &= e_0 + e_1r + e_2r^2 + e_3r^3 \\ \kappa(r) &= f_0 + f_1r + f_2r^2 + f_3r^3 \end{aligned} \quad (2)$$

where  $r$  is the row index in the image, and  $X_s(r)$ ,  $Y_s(r)$ ,  $Z_s(r)$ ,  $\varphi(r)$ ,  $\omega(r)$ , and  $\kappa(r)$  are the EO parameters of the image row  $r$ .  $a_i, \dots, f_i$  ( $i = 0, 1, 2, 3$ ) are the coefficients of the polynomials.

After linearization of Eqs. (1) and (2), the observation equation system for the combined block adjustment of Chang'E-2 imagery and LOLA data can be represented in matrix form as the following:

$$\begin{aligned} V_1 &= AX_1 - L_1, P_1 \\ V_2 &= BX_1 + CX_2 - L_2, P_2 \\ V_3 &= BX_1 + CX_3 - L_3, P_3 \\ V_4 &= DX_2 - L_4, P_4 \\ V_5 &= DX_1 - L_5, P_5 \end{aligned} \quad (3)$$

The observation equation system includes the following five types of observation equations. The first corresponds to the arrow marked with ① in Fig. 2, which is the pseudo observation equation for the image EO parameters.  $X_1$  is the vector of corrections to the unknown coefficients  $a_i, \dots, f_i$  ( $i = 0, 1, 2, 3$ ) in the polynomials in Eq. (2). By the term "pseudo", it means the measurements are estimated instead of real measurements (such as the precisely matched tie points) in other types of observations and they are used as initial input of the unknowns. The pseudo observations for the image EO parameters are selected from the initial image EO parameters, which are discrete samples along the row direction of the image. The refined EO parameters are assumed to fluctuate around them.

The second observation equation corresponds to the arrows marked with ② in Fig. 2, which relate to the intra- and inter-strip tie points identified from the images. Intra-strip tie points are identified within each image strip, and inter-strip tie points are identified in the overlapping areas of two neighbor image strips. For the observations of the intra- and inter-strip tie points, they connect the 3D ground points and their image measurements by the EO parameters as indicated in Eqs. (1) and (2).  $X_2$  is the vector of corrections to the unknown ground coordinates of the tie points that are simultaneously solved with  $X_1$ .

The third observation equation corresponds to the arrow marked with ③ in Fig. 2, which is for the LOLA points.  $X_3$  is the vector of corrections to LOLA points. It should be noted that, the adjustment to LOLA points can be controlled based on their corresponding weights. Because of the superior accuracy of LOLA points, they can be awarded with large weights, so that they will only be adjusted slightly in local regions. Given infinite weights they will not change during the block adjustment and act as control points. The image coordinates of the LOLA points are initially derived by back-projecting the LOLA points onto the stereo images using the initial image EO parameters. The initially determined image coordinates of the LOLA points on the stereo images are not necessarily the same homologous points due to the inaccurate image EO parameters and inconsistencies between the two data sets. However, they will be corrected in the adjustment process.

The fourth equation corresponds to the arrow marked with ④ in Fig. 2, which is a pseudo observation equation related to a local surface constraint in the adjustment model. The fifth observation equation corresponds to the arrow marked with ⑤ in Fig. 2, which is the orbit height constraint. These two constraints are specifically designed in the block adjustment model to help reduce the inconsistencies between the Chang'E-2 imagery and LOLA data. The details are described in Section 4.4.

In the observation equation system (Eq. (3)), the coefficient matrix  $A$ ,  $B$ ,  $C$  and  $D$  contains partial derivatives with respect to the unknown parameters.  $P_i$  ( $i = 1, 2, 3, 4, 5$ ) represents different weight for each observation, which will be described in detail in Section 4.5. The block adjustment is processed iteratively based on a least squares approach. In each iteration the corrections are added to the unknown parameters, so that the precise values of the unknown parameters are finally obtained.

#### 4.3. Intra- and inter-strip tie points determination

Two types of tie points, intra- and inter-strip tie points, are employed in the block adjustment. As illustrated in Fig. 3, intra-strip tie points are identified within the stereo images (forward- and backward-looking images) of each strip. They are used in the block adjustment to eliminate the internal inconsistency of intra-strip stereo. Inter-strip tie points are identified in the overlapping areas of two neighbor image strips and measured in both image strips. The overlapping areas between any two adjacent orbits range from 30% to 50% for the Chang'E-2 imagery. The inter-strip tie points are used in the block adjustment to eliminate the disagreement between two adjacent image strips.

Automatic interest point detection and matching methods (Wu et al., 2012, 2011b; Zhu et al., 2007a, 2007b) are employed for feature point matching, and intra- and inter-strip tie points are selected from the matched feature points and checked for even distribution. There are hundreds of intra-strip tie points used in the block adjustment and they are evenly distributed on the

images, including the overlapping areas between two neighbor image strips. Dozens of inter-strip tie points are used in the block adjustment, and they are evenly distributed within the overlapping areas of any two neighbor image strips.

#### 4.4. Constraints in the block adjustment

As mentioned previously, there are significant inconsistencies between the topographic models derived from the Chang'E-2 imagery and LOLA data separately (e.g., about 300 m difference in elevation in the Sinus Iridum area). Therefore, the following two constraints are specifically designed in the block adjustment approach to reduce the inconsistencies between these two data sets.

##### 4.4.1. LOLA data used as local surface constraint

In the traditional photogrammetric processing of stereo images, including the block adjustment for the generation of digital topographic models, ground control points have generally been used as ground truth to improve the accuracy of the derived topographic models. On the lunar surface, very few precisely known points can serve as classical ground control points, but a large number of ground points were measured by LOLA. However, the exact image coordinates of these LOLA points cannot be determined in the stereo images. Therefore, it is not possible to use the LOLA points as normal ground control points in a block adjustment. Instead, a local surface constraint was developed to incorporate the LOLA points to provide constraints in the block adjustment of Chang'E-2 images.

The basic idea of this local surface constraint is that the ground positions of the intra- and inter-strip tie points on the Chang'E-2 images obtained through a space intersection using the image EO parameters should be consistent with a local surface determined by the nearby LOLA points. The local surface constraint can be represented by the following equation:

$$\sqrt{X_T^2 + Y_T^2 + Z_T^2} - R - H_L = 0 \quad (4)$$

where  $X_T$ ,  $Y_T$ , and  $Z_T$  are the ground positions of the tie points in the lunar geocentric coordinate system originated at the spheroid center,  $R$  is the radius of the Moon (1737.4 km), and  $H_L$  is the height at the location of  $X_T$ ,  $Y_T$  interpolated from the nearby LOLA points. After linearization of Eq. (4), it can be represented in matrix form which is the fourth observation equation in Eq. (3). With this constraint an improvement of the height derived from the Chang'E-2 images can be expected.

From the experimental analysis in this study, it is noticed that without this local surface constraint, it is difficult to achieve convergence in the block adjustment process between the Chang'E-2 imagery and the LOLA data due to the large inconsistencies between these two data sets and the lack of ground control points. By adding this local surface constraint, the block adjustment model is able to effectively improve the heights derived from the Chang'E-2 images to achieve results close to those of the LOLA data.

##### 4.4.2. Orbit height constraint

The above mentioned local surface constraint has the potential to improve the heights derived from the Chang'E-2 images. However, improvements in planimetry can only be expected if there are different local terrain slopes at the different surfaces determined by the LOLA points, an element which is hard to explicitly incorporate in the block adjustment model. Moreover, in the block adjustment process the EO parameters of the Chang'E-2 images are adjusted simultaneously and erroneous results in planimetry may exist, especially considering the large inconsistencies between the Chang'E-2 images and LOLA data and between multiple strips of

Chang'E-2 images. The imposition of an explicit constraint on EO parameters is considered to remedy this situation; this is the orbit height constraint.

Because the Chang'E-2 spacecraft had a circular orbit of 100 km when collecting the images with 7 m spatial resolution, the orbit height constraint is defined as follows:

$$\sqrt{X_S^2 + Y_S^2 + Z_S^2} - R - H_O = 0 \quad (5)$$

where  $X_S$ ,  $Y_S$ , and  $Z_S$  are the translation elements of image EO parameters representing the projective center of the camera,  $R$  is the radius of the Moon (1737.4 km), and  $H_O$  is the height of the Chang'E-2 orbit (100 km). This orbit height constraint indicates that the length of the vector determined by the translation elements of image EO parameters should be equal to the constant orbit height of the Chang'E-2 spacecraft plus the radius of the Moon. After linearization of Eq. (5), it can be represented in matrix form that is the fifth observation equation in Eq. (3).

#### 4.5. Weight determination in the block adjustment

The weights  $P_i$  ( $i = 1, 2, 3, 4, 5$ ) in the block adjustment model (Eq. (3)) indicate the contribution of each type of observation. They are generally determined by the *a priori* standard deviation  $\sigma_i$  ( $i = 1, 2, 3, 4, 5$ ) for each type of observation. More specifically, the weight  $P_i$  can be determined by the reciprocal of  $\sigma_i^2$ .

Although the determination of  $\sigma_i$  for each type of observation is arbitrary, it should be based on appropriate assumptions. For the  $\sigma_1$  of the first observation equation relating to the initial EO parameters, 1000 m is chosen for the translation elements ( $X, Y, Z$ ) and 0.028 gon for the rotation elements ( $\varphi, \omega, \kappa$ ) following Bostelmann et al. (2012) in the experiments of the HRSC imagery. For the  $\sigma_2$  of the second observation equation regarding the tie points, one third of a pixel is chosen because this is the paradigm in determining the weight for tie point observations. For the  $\sigma_3$  of the third observation equation regarding the LOLA points,  $\sigma_3 = 10$  pixels is used based on the practical experimental analysis in this research and Yoon and Shan (2005). For the  $\sigma_4$  of the fourth observation equation about the local surface constraint, generally  $\sigma_4 = 10$  m is used in this research considering the LOLA points are very accurate, which indicates that the local surface determined by the nearby LOLA points has the *a priori* standard deviation of 10 m. For the  $\sigma_5$  of the fifth observation equation relating to the orbit height constraint, the orbit height constraint should be quite loose because maximal  $\pm 15$  km deviation is expected for the nominal 100 km circular orbit of the Chang'E-2 spacecraft (Zhou and Yang, 2010). Therefore,  $\sigma_5 = 5000$  m is suitable supposing that the deviation accords with uniform distribution between  $[-15, 15]$  km.

It should be noted that from previous experiences in photogrammetry (Yoon and Shan, 2005; Wu et al., 2011a), moderate changes in weight magnitude will yield the same results from the adjustment model.

### 5. Experimental analysis

#### 5.1. Experiments in the Sinus Iridum area

Sinus Iridum (Latin for "Bay of Rainbows") is a plain area that forms a northwestern extension to the Mare Imbrium. The Chinese first lunar lander/rover Chang'E-3 is planned to land in the Sinus Iridum area in 2013. In this study, the experimental area in Sinus Iridum covered a region of  $18^\circ$  to  $25.7^\circ$  W and  $42^\circ$  to  $46.3^\circ$  N. The topography in this area is relatively flat with a maximum elevation difference of about 1 km. The experimental data includes six strips of Chang'E-2 imagery with orbit numbers from 0570 to 0575 and 1,740,036 LOLA points. The size for each image is



**Fig. 4.** LOLA points overlaid on the Chang'E-2 image mosaic in the Sinus Iridum area.

$6144 \times 18,000$  pixels and there is an overlap of about 45% between two neighbor image strips. Fig. 4 shows the LOLA points overlaid on the Chang'E-2 image mosaic for this area. It should be noted that, not all of the LOLA points are used in the block adjustment due to the unaffordable computation cost. Empirically, 100–300 well distributed LOLA points for each image strip are enough for the combined block adjustment. A DEM interpolated from all the LOLA points is used for comparison purpose.

A primary objective of the proposed combined block adjustment is to reduce the inter-strip inconsistency induced by the errors in the initial EO parameters of the Chang'E-2 imagery. Fig. 5 gives a qualitative validation by visually comparing the DEMs generated using the image EO parameters before and after the combined block adjustment. For DEM generation, a dense image matching method (Wu et al., 2011b; 2012) was used to obtain dense point matches from the Chang'E-2 stereo images, and the ground positions of the matched points were calculated through a space intersection using the image EO parameters, from which DEMs with 20 m spatial resolution were interpolated using the Kriging method. As shown in Fig. 5(a), the DEM generated using the initial image EO parameters shows rough areas in the overlapping regions of the Chang'E-2 image strips, which are mainly caused by the inter-strip inconsistency of the Chang'E-2 imagery. These rough areas are removed in the DEM generated using the refined image EO parameters after the combined block adjustment as shown by the smooth terrain surface in Fig. 5(b).

To quantitatively analyze the performance of the combined block adjustment approach, hundreds of quadruple matched points in the overlapping areas are selected as check points. The ground positions of these check points are obtained through space intersection using the EO parameters of the Chang'E-2 images in the first strip, and then back-projected onto the neighbor strip of images using their corresponding EO parameters. The discrepancies between the original image coordinates of the check points and the back-projected coordinates are plotted on the Chang'E-2 imagery mosaics as shown in Fig. 6.

Fig. 6(a) illustrates the image residual vectors before the combined block adjustment that are exaggerated 10 times for better visual comparison. Fig. 6(b) shows the residual vectors after the combined block adjustment that are exaggerated 100 times. Detailed statistics are summarized in Table 1, including mean absolute error (MAE), Maximum, Minimum, and StDev (standard deviation). Two improvements are obtained from the combined block adjustment. First, the mean absolute image residuals are reduced

**Table 1**

Statistics of the image residuals before and after the combined block adjustment in the Sinus Iridum area.

		MAE (pixels)	Max (pixels)	Min (pixels)	StDev (pixels)
(a) Image residuals before the combined block adjustment					
0570–0571	Residual X	35.378	61.898	-69.553	25.364
	Residual Y	13.332	33.269	-2.291	7.882
	Residual vector	38.756	73.826	1.392	18.234
0571–0572	Residual X	11.584	15.003	-44.286	11.575
	Residual Y	6.602	13.443	-12.802	5.673
	Residual vector	14.121	46.281	0.769	9.411
0572–0573	Residual X	17.520	76.444	-27.546	21.399
	Residual Y	8.112	14.966	-5.568	5.231
	Residual vector	20.897	76.452	1.014	12.326
0573–0574	Residual X	16.634	46.776	-49.230	19.561
	Residual Y	9.037	7.783	-22.248	7.111
	Residual vector	20.867	49.243	1.293	10.144
0574–0575	Residual X	13.526	36.214	-35.094	16.560
	Residual Y	10.914	20.353	-21.825	9.253
	Residual vector	18.400	41.934	2.682	9.390
(b) Image residuals after the combined block adjustment					
0570–0571	Residual X	0.272	1.089	-1.070	0.341
	Residual Y	0.117	0.505	-0.526	0.152
	Residual vector	0.322	1.091	0.011	0.198
0571–0572	Residual X	0.315	1.454	-0.989	0.391
	Residual Y	0.171	0.984	-0.981	0.237
	Residual vector	0.393	1.469	0.017	0.239
0572–0573	Residual X	0.320	1.388	-1.118	0.402
	Residual Y	0.191	0.750	-0.898	0.250
	Residual vector	0.409	1.401	0.016	0.245
0573–0574	Residual X	0.285	1.464	-0.950	0.353
	Residual Y	0.310	1.539	-0.729	0.405
	Residual vector	0.467	1.621	0.016	0.270
0574–0575	Residual X	0.320	1.202	-1.561	0.409
	Residual Y	0.321	1.334	-1.539	0.440
	Residual vector	0.502	2.054	0.028	0.334

from 14–39 pixels before the block adjustment to 0.3–0.5 pixels after the block adjustment while the standard deviations are reduced from 9–18 pixels to about 0.2 pixels. Second, residual vectors before the combined block adjustment contain obvious systematic errors. The errors are predominately biased in the side overlap direction and have a legibly diffuse pattern as addressed by the blue rectangles in Fig. 6(a). The bias in residual error can also be quantitatively gauged from the average residual error before the

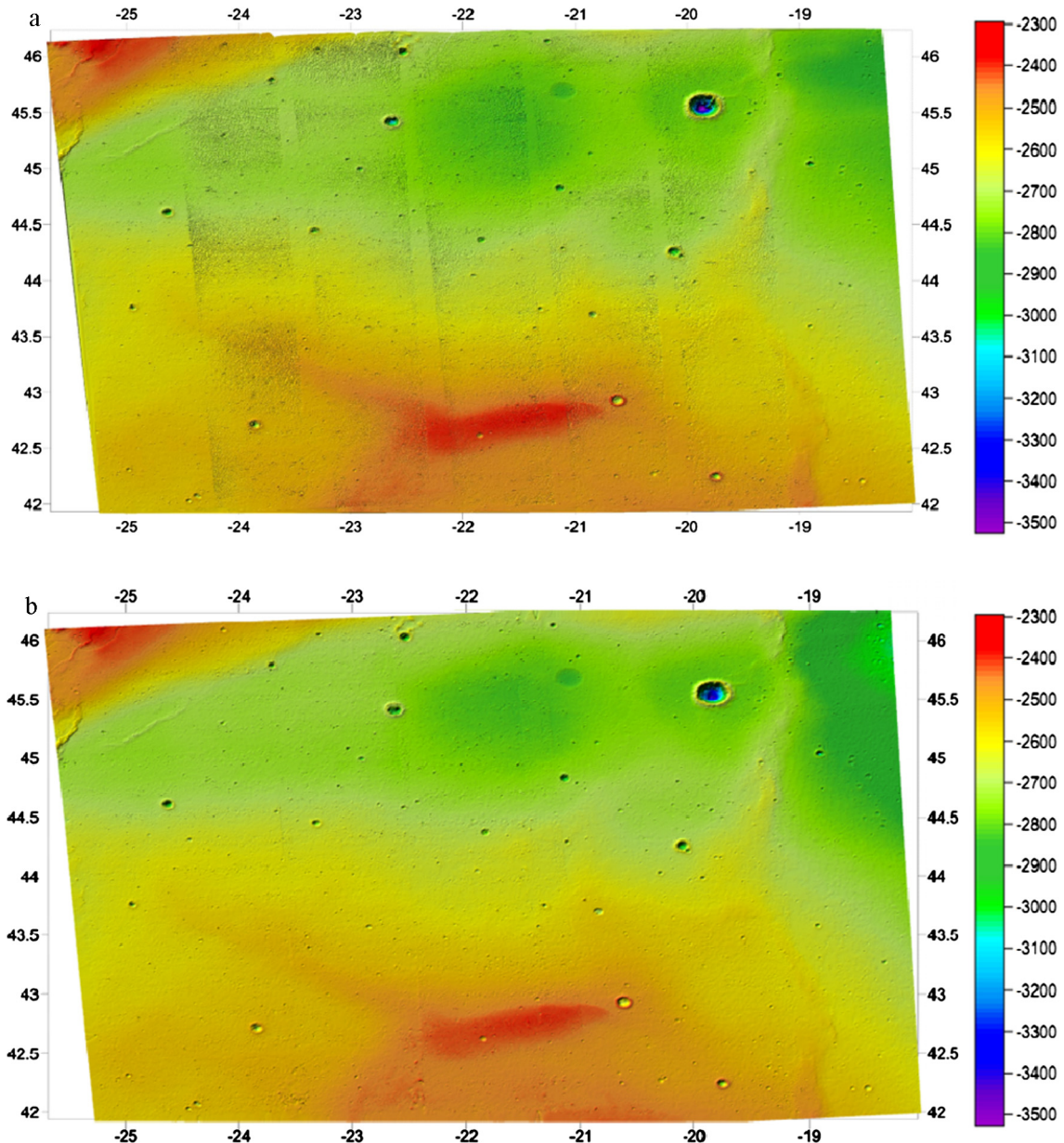


**Fig. 5.** Comparison of DEMs before and after combined block adjustment in the Sinus Iridium area. (a) DEM generated using initial image EO parameters and (b) DEM generated using image EO parameters refined by combined block adjustment.

combined block adjustment in X and Y direction as shown in Table 1. After the combined block adjustment the residual vectors are generally randomly distributed and no clearly diffuse pattern exists.

With the combined block adjustment, the DEM generated from the Chang'E-2 imagery is expected to align well with the DEM directly interpolated from the LOLA points. To evaluate the fit between these two DEMs, four reference lines are selected for profile comparison as shown in Fig. 7, of which two are along the North-South direction and the other two are along the East-West direction.

Fig. 8 shows that the profiles derived from the LOLA DEM and Chang'E-2 DEM are visually quite consistent. The statistics for the elevation differences between the corresponding profiles are listed in Table 2. The fit between the two DEMs can be denoted by the MAE of the elevation differences, which is about 10 m except for reference line 2. The abnormal 20.06 m in reference line 2 is due to the large discrepancies in the largest crater which has a diameter over 500 m. The reason for the large discrepancy may be a lack of matched points inside the crater on the Chang'E-2 imagery, so that the interpolated DEM is shallower than the DEM derived from LOLA points in the crater region. Furthermore, the spikes in the profiles as can be noticed from Figs. 8(c) and 8(d) may be occasionally sampled points on low hills or shallow craters. In fact, the MAE by a maximum about 20 m between the two profiles can be considered as acceptable.

**Table 2**

Statistics for the elevation differences between the profiles derived from LOLA DEM and Chang'E-2 DEM in the Sinus Iridum area.

	MAE (m)	Max (m)	Min (m)	StDev (m)
Reference #1	6.721	40.233	-92.989	9.879
Reference #2	20.060	198.521	-518.685	69.626
Reference #3	11.255	39.464	-61.888	14.958
Reference #4	10.835	49.483	-66.688	9.981

eter over 500 m. The reason for the large discrepancy may be a lack of matched points inside the crater on the Chang'E-2 imagery, so that the interpolated DEM is shallower than the DEM derived from LOLA points in the crater region. Furthermore, the spikes in the profiles as can be noticed from Figs. 8(c) and 8(d) may be occasionally sampled points on low hills or shallow craters. In fact, the MAE by a maximum about 20 m between the two profiles can be considered as acceptable.

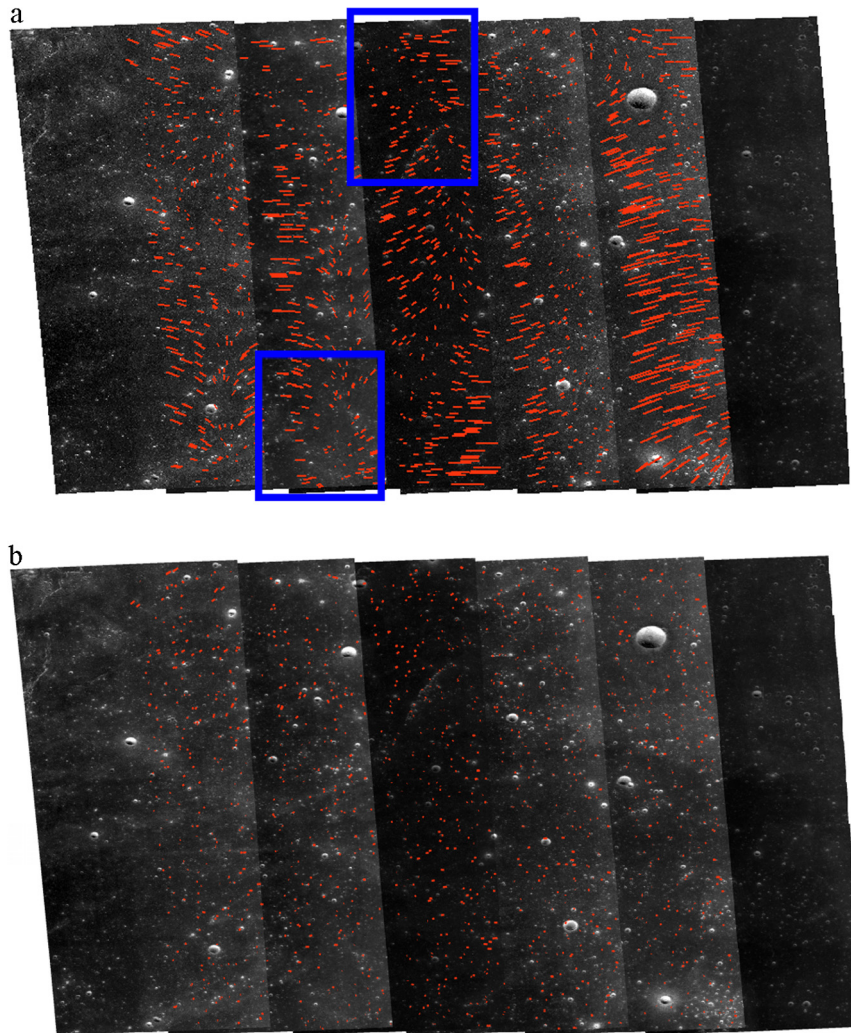


**Fig. 6.** Residual vectors of the check points overlaid on Chang'E-2 image mosaics in the Sinus Iridum area. (a) Residuals before the combined block adjustment (exaggerated 10 $\times$ ) and (b) residuals after the combined block adjustment (exaggerated 100 $\times$ ).

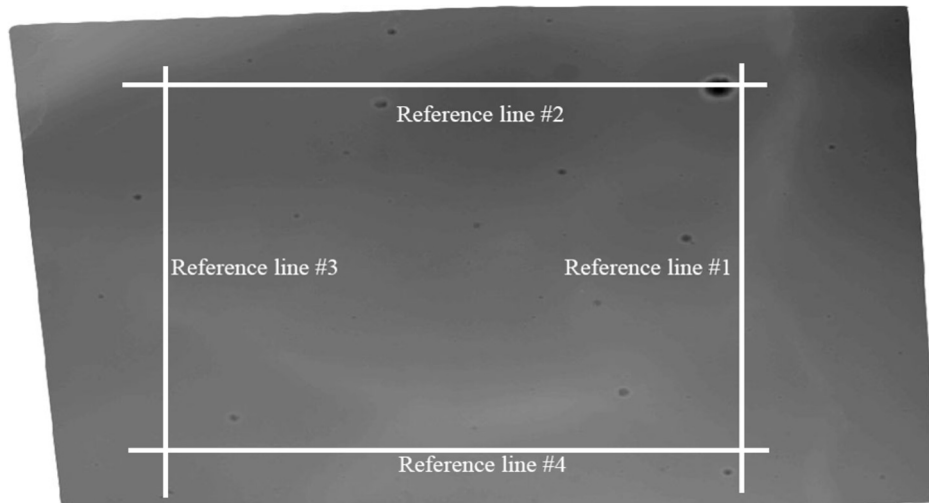


**Fig. 7.** Reference lines for profile comparison in the Sinus Iridum area.

### 5.2. Experiments in the Apollo 15 landing area

The Apollo 15 landing area is located at the foot of the Apennine Mountain range. The experimental area in this research covered a region of 0.15° to 4° E and 24° to 28° N, including three

strips of Chang'E-2 imagery with orbit number from 0550 to 0552 and 105,535 LOLA points. The size for each image is 6144 × 18,000 pixels, and there is about 30% overlap between two neighbor image strips. Unlike the previous experimental area in the Sinus Iridum area, the topography in this area is rugged and contains

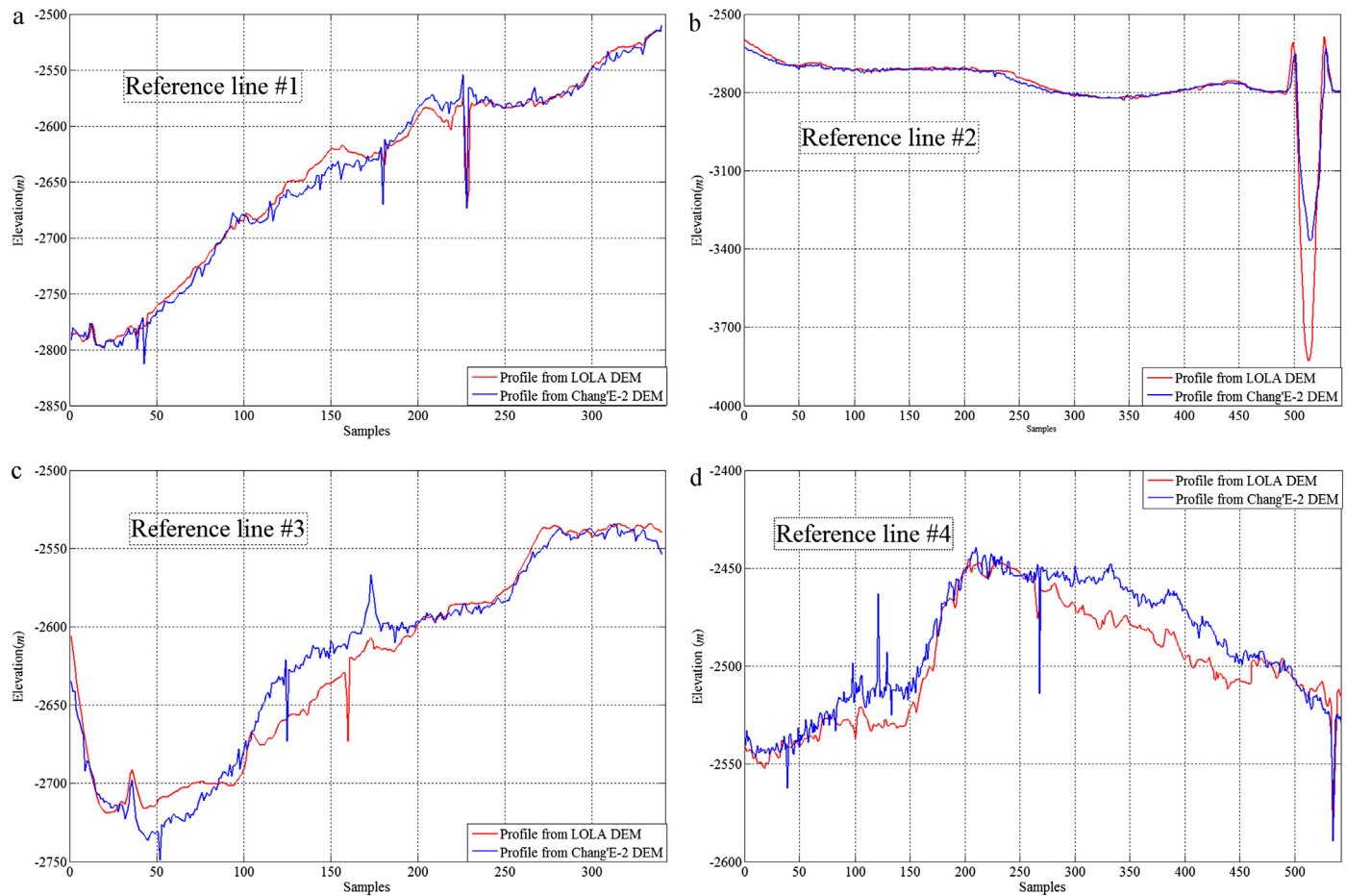


**Fig. 8.** Profiles derived from LOLA DEM and Chang'E-2 DEM in the Sinus Iridium area. (a) Profiles for reference line 1, (b) profiles for reference line 2, (c) profiles for reference line 3, and (d) profiles for reference line 4.

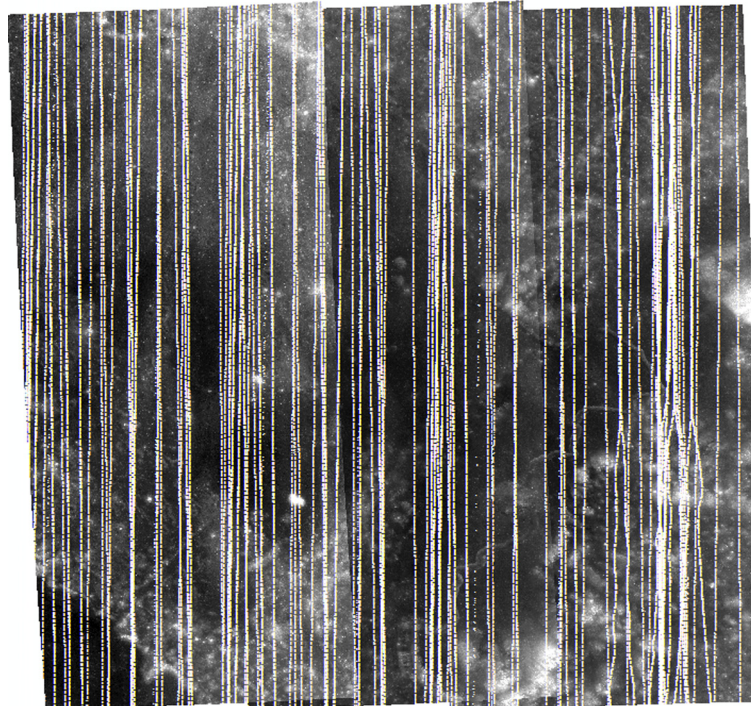


**Fig. 9.** LOLA points overlaid on the Chang'E-2 image mosaic in the Apollo 15 landing area.

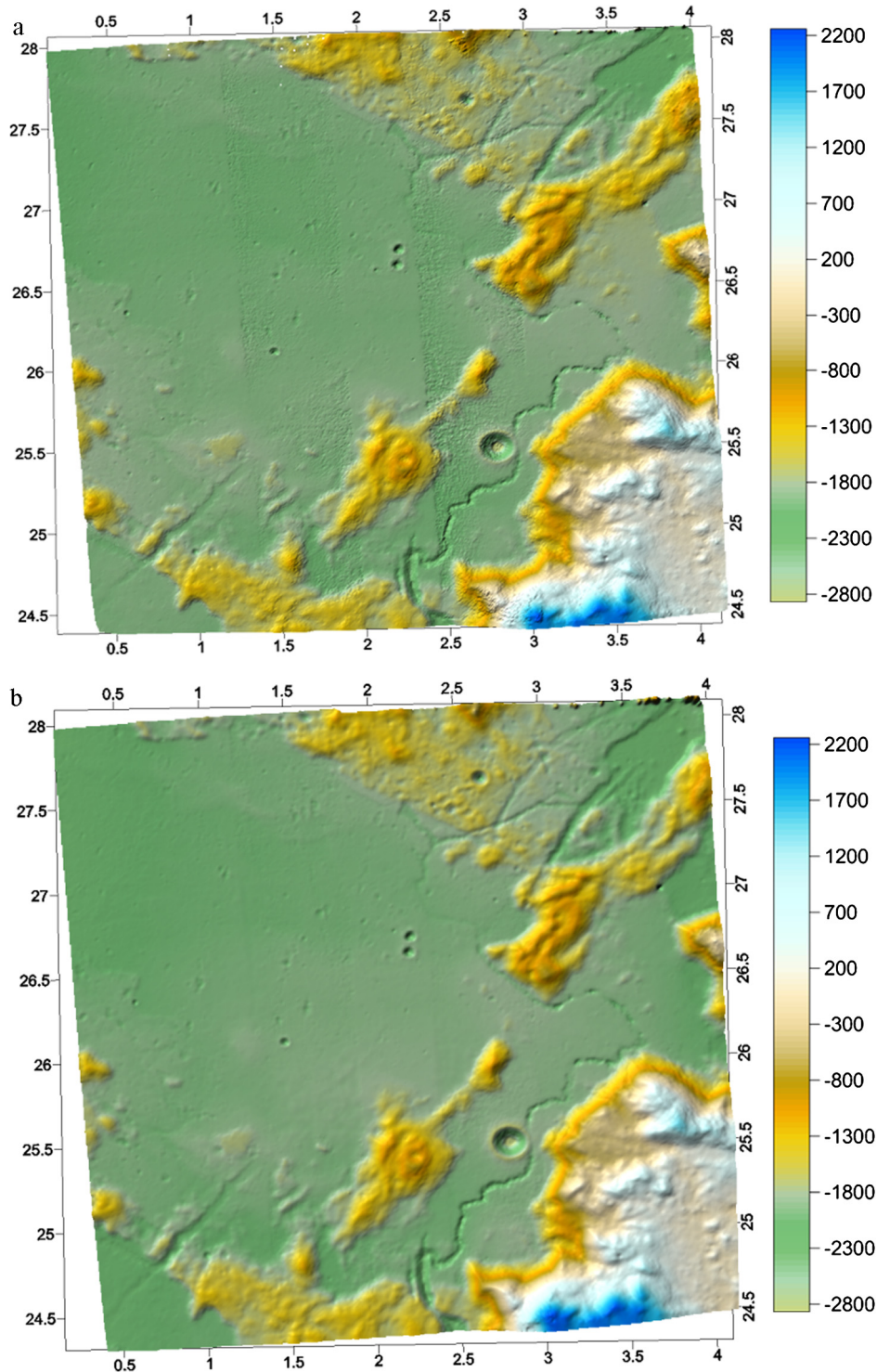


**Fig. 10.** Comparison of DEMs before and after combined block adjustment in the Apollo 15 landing area. (a) DEM generated using initial image EO parameters and (b) DEM generated using image EO parameters refined by combined block adjustment.

various terrain features including flat lands, continuous mountains, long gullies, and craters. The maximum elevation difference in this area is about 6 km. Fig. 9 shows the LOLA points overlaid on the Chang'E-2 image mosaic in this area.

Similar to the previous scenario, two DEMs are generated using the EO parameters of the Chang'E-2 images before and after the combined block adjustment. Fig. 10 provides a visual comparison between the two DEMs. Roughness in the overlapping area of the image strips before the combined block adjustment as can be seen

in Fig. 10(a) has been removed after the combined block adjustment as shown in Fig. 10(b). As can be seen from Fig. 10(a), the inconsistency within the right two image strips (0550 and 0551) is more serious than that between the left two image strips (0551 and 0552), which results in a more severe and larger rough area. This can be quantitatively analyzed based on the image residuals.

Fig. 11(a) shows the image residual vectors of the quadruple tie points before the combined block adjustment exaggerated 10 times. Fig. 11(b) shows the image residual vectors after the

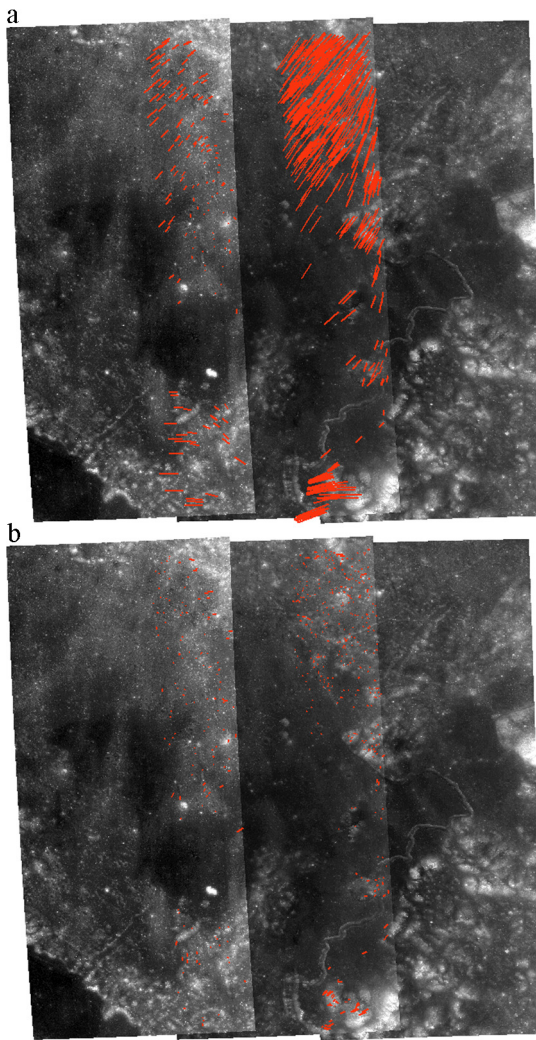


**Fig. 11.** Residual vectors of the check points overlaid on Chang'E-2 image mosaics in the Apollo 15 landing area. (a) Residuals before the combined block adjustment (exaggerated 10 $\times$ ) and (b) residuals after the combined block adjustment (exaggerated 100 $\times$ ).

combined block adjustment exaggerated 100 times. The corresponding statistics are listed in Table 3. It can be seen from Fig. 11 that the residual vectors between the right two image strips (0550 and 0551) are much longer than those of the left two strips (0551 and 0552). The average image residual for the right two image strips is about 68 pixels, compared with 18.5 pixels for the left two image strips before the combined block adjustment. This explains the different magnitude of roughness shown in Fig. 11(a). Furthermore, the same two types of systematic error, which are due to directional bias and diffuse patterns as exposed in the Sinus Iridum area, are also seen in Fig. 11(a), where they are more evident.

After the combined block adjustment, the quality of the EO parameters of the Chang'E-2 images has been improved at least in three aspects. First, the image residual vectors for both overlapping areas (0550–0551 and 0551–0552) have decreased drastically from 18–68 pixels to the sub-pixel level, as listed in Table 3. The standard deviations for the two overlapping areas have also been reduced from over 10 pixels to the sub-pixel level. This indicates that the inconsistencies in the overlap areas are significantly reduced. Second, different levels of inconsistency between the two overlapping areas have been leveraged to and reach to about the same MAE of the residuals. Therefore, the DEM generated using the EO parameters after the combined block adjustment will obtain over-

**Table 3**

Statistics of the image residuals before and after the combined block adjustment in the Apollo 15 landing area.

		MAE (pixels)	Max (pixels)	Min (pixels)	StDev (pixels)
(a) Image residuals before the combined block adjustment					
0550–0551	Residual X	40.838	116.390	0.876	17.077
	Residual Y	51.408	3.483	-73.646	14.752
	Residual vector	67.863	116.442	16.408	14.599
0551–0552	Residual X	14.270	54.515	-1.693	11.400
	Residual Y	10.296	23.596	-25.648	10.166
	Residual vector	18.479	54.612	0.217	11.574
(b) Image residuals after the combined block adjustment					
0550–0551	Residual X	0.535	2.931	-7.295	0.869
	Residual Y	0.459	3.443	-4.436	0.696
	Residual vector	0.793	7.328	0.013	0.787
0551–0552	Residual X	0.569	2.203	-3.487	0.809
	Residual Y	0.588	2.340	-2.826	0.760
	Residual vector	0.911	4.200	0.039	0.633

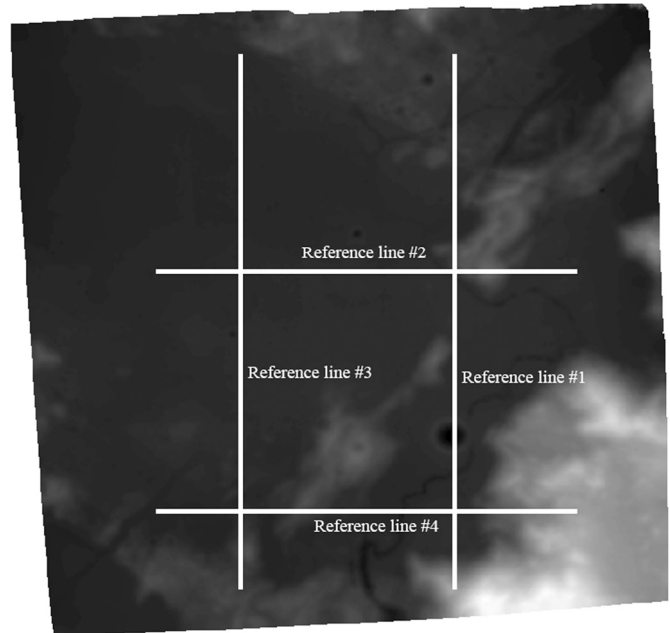


**Fig. 12.** Reference lines for profile comparison in Apollo 15 landing area.

all smoothness instead of the previous imbalance in consistency. Third, systematic errors have been eliminated as the directional bias and diffuse pattern of the residual vectors is no longer visible in Fig. 11(b).

To evaluate the performance of the combined block adjustment, the DEM generated from the Chang'E-2 imagery after the combined block adjustment is compared with the DEM directly interpolated from the LOLA points. Four reference lines are selected for profile comparison, as shown in Fig. 12, of which two are along the North–South direction and the other two are along the East–West direction.

Fig. 13 shows that the profiles derived from LOLA DEM and Chang'E-2 DEM are generally quite consistent. The statistics for the elevation differences are listed in Table 4. The MAE of the elevation difference for the four reference lines ranges from 15 to 42 m. The results for the Apollo 15 landing area are arguably worse than those for the Sinus Iridum area. This may be related to the complex terrain features and huge fluctuation in elevation in the Apollo 15 landing area. The elevation range is typically 300 m for the Sinus Iridum area as shown in Fig. 8 while the range is 3000 m for profiles in the Apollo 15 landing area. In addition, almost all of the

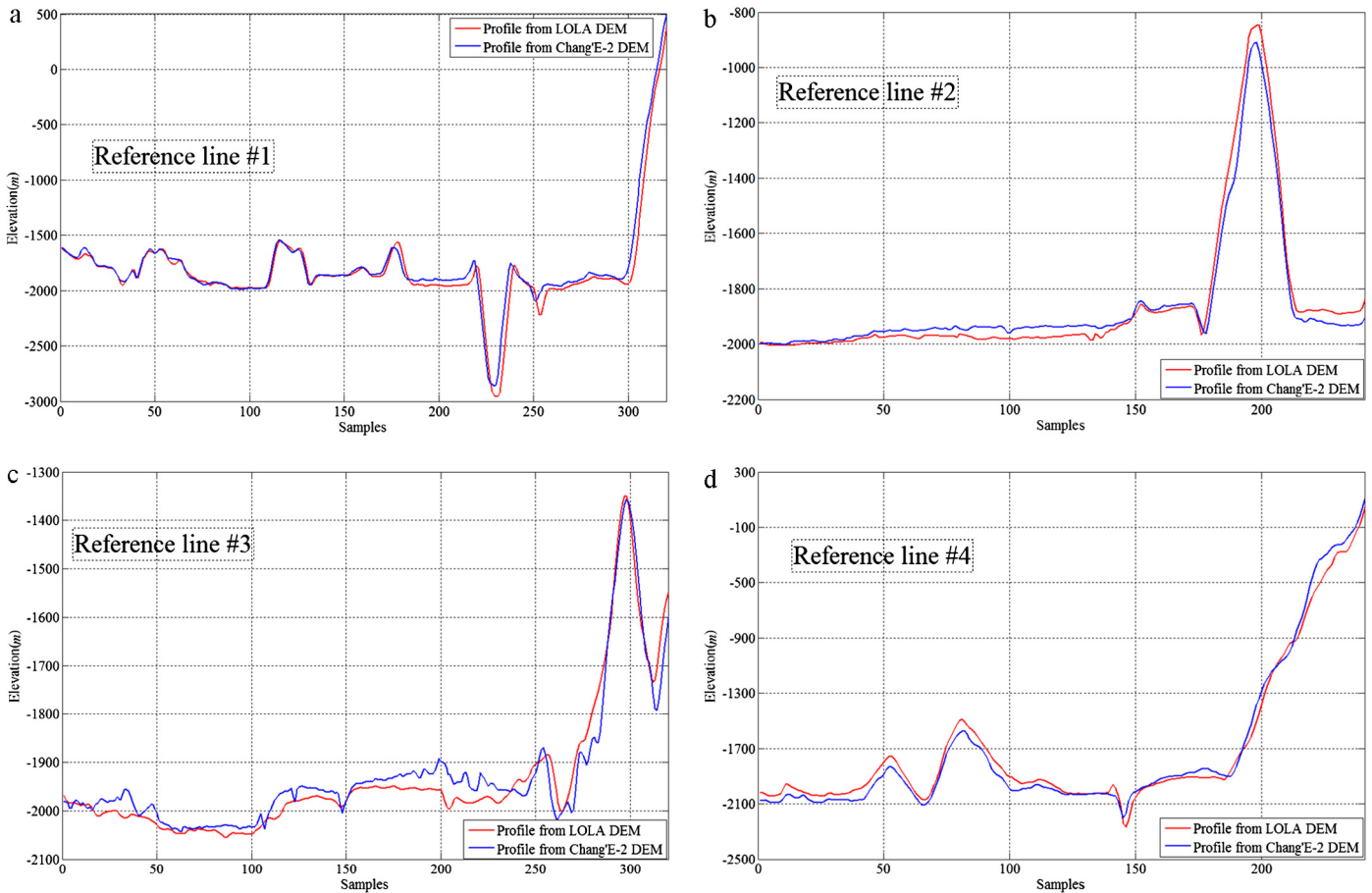


**Fig. 13.** Profiles derived from LOLA DEM and Chang'E-2 DEM in the Apollo 15 landing area. (a) Profiles for reference line 1, (b) profiles for reference line 2, (c) profiles for reference line 3 and (d) profiles for reference line 4.

**Table 4**

Statistics of the elevation differences between the profiles derived from LOLA DEM and Chang'E-2 DEM in the Apollo 15 landing area.

	MAE (m)	Max (m)	Min (m)	StDev (m)
Reference #1	41.175	200.077	-395.013	56.239
Reference #2	22.817	160.269	-49.925	42.709
Reference #3	15.369	106.365	-79.838	31.979
Reference #4	21.742	97.421	-175.407	39.908

obvious terrain features that are revealed in the profiles can be registered well enough free of impact from large elevation range.

## 6. Concluding remarks

This paper presents a combined block adjustment approach for the integration of Chang'E-2 imagery and LOLA data for precision lunar topographic modeling. The approach incorporates LOLA data to improve the EO parameters of the Chang'E-2 imagery and uses two particular constraints to minimize the inconsistencies between the overlapping Chang'E-2 images and the inconsistencies between the Chang'E-2 and LOLA data sets. The performance of the developed combined block adjustment approach was evaluated using multiple strips of Chang'E-2 imagery and LOLA data in the Sinus Iridum area and the Apollo 15 landing area. In both experimental areas, the mean absolute image residuals were drastically reduced from tens of pixels before the block adjustment to sub-pixel level (0.3–0.5 pixels for the Sinus Iridum area and 0.8–0.9 pixels for the Apollo 15 landing area) after the block adjustment, while the standard deviations were reduced from over 10 pixels to sub-

pixel level as well (about 0.2 pixels for the Sinus Iridum area and 0.8 pixels for the Apollo 15 landing area). DEMs with 20 m resolution were generated based on the improved EO parameters of the Chang'E-2 imagery after the combined block adjustment. Comparison of the Chang'E-2 DEM with the LOLA DEM showed a good level of consistency.

The combined block adjustment approach developed in this study was able to integrate cross-mission and cross-sensor lunar orbiter imagery and laser altimeter data for precision lunar topographic modeling, which will permit the full comparative and synergistic use of lunar topographic data sets from different sources. This cross-sensor and cross-mission data integration strategy can also be used in other similar applications on Earth, Mars, and beyond.

## Acknowledgements

The authors would like to thank the National Astronomical Observatories of the Chinese Academy of Sciences for providing the Chang'E-2 imagery. The work described in this study was supported by a grant from the Research Grants Council of Hong Kong (Project No: PolyU 5312/10E) and a grant from the National Natural Science Foundation of China (Project No: 91338110). The work was also supported by a project from the China Academy of Space Technology.

## References

- Albertz, J., Attwenger, M., Barrett, J., Casley, S., Dorninger, P., Dorrer, E., Ebner, H., Gehrke, S., Giese, B., Gwinner, K., 2005. HRSC on Mars express-photogrammetric and cartographic research. Photogramm. Eng. Remote Sens. 71 (10), 1153–1166.

- Anderson, F.S., Parker, T.J., 2002. Characterization of MER landing sites using MOC and MOLA. In: Proceedings, 33rd Lunar and Planetary Science Conference. League City, Texas, March 11–15.
- Araki, H., Tazawa, S., Noda, H., Ishihara, Y., Goossens, S., Sasaki, S., Kawano, N., Kamiya, I., Otake, H., Oberst, J., Shum, C., 2009. Lunar global shape and polar topography derived from Kaguya-LALT laser altimetry. *Science* 323, 897–900.
- Arya, A.S., Rajasekhar, R.P., Thangjam, G., Ajai Kumar, A.S.K., 2011. Detection of potential site for future human habitability on the Moon using Chandrayaan-1 data. *Curr. Sci.* 100 (4), 524–529.
- Bostelmann, J., Schmidt, R., Heipke, C., 2012. Systematic bundle adjustment of HRSC image data. *Int. Arch. Photogramm. Remote Sens. Spat. Inf. Sci.* XXXIX-B4, 301–306.
- Brown, D.C., 1968. A unified lunar control network. *Photogramm. Eng.* 34 (12), 1272–1292.
- Brown, D.C., 1976. The bundle adjustment – Progress and prospects. *Int. Arch. Photogramm.* 21 (3), 33 p.
- Burns, K.N., Speyerer, E.J., Robinson, M.S., Tran, T., Rosiek, M.R., Archinal, B.A., Howington-Kraus, E., the LROC Science Team, 2012. Digital elevation models and derived products from LROC NAC stereo observations. *Int. Arch. Photogramm. Remote Sens. Spat. Inf. Sci.* XXXIX-B4, 483–488.
- Cramer, M., Haala, N., 2010. DGPF project: Evaluation of digital photogrammetric aerial-based imaging systems – Overview and results from the pilot center. *Photogramm. Eng. Remote Sens.* 76 (9), 1019–1029.
- Di, K., Hu, W., Liu, Y., Peng, M., 2012. Co-registration of Chang'E-1 stereo images and laser altimeter data with crossover adjustment and image sensor model refinement. *Adv. Space Res.* 50 (12), 1615–1628.
- Doyle, F.J., Elassel, A.A., Lucas, J.R., 1976. Experiment S-213 selenocentric geodetic reference system. NASA STI, Final Report B28631-000A. National Oceanic and Atmospheric Administration, Rockville, MD.
- Ebner, H., Strunz, G., Colomina, I., 1991. Block triangulation with aerial and space imagery using DTM as control information. CSM-ASPRS Auto-Carto 10, Annual Convention, Technical papers, Baltimore, March 25–29, Vol. 5, pp. 76–85.
- Garvin, J.B., Sakimoto, S., Schnetzler, C., Frawley, J.J., 1999. Global geometric properties of martian impact craters: a preliminary assessment using Mars Orbiter Laser Altimeter (MOLA). In: The Fifth International Conference on Mars. July 18–23, Pasadena, CA.
- Gwinner, K., Scholten, F., Spiegel, M., Schmidt, R., Giese, B., Oberst, J., Heipke, C., Jaumann, R., Neukum, G., 2009. Derivation and validation of high-resolution digital terrain models from Mars Express HRSC-Data. *Photogramm. Eng. Remote Sens.* 75 (9), 1127–1142.
- Haruyama, J., Hara, S., Hioki, K., Iwasaki, A., Morota, T., Ohtake, M., Matsunaga, T., Araki, H., Matsumoto, K., Ishihara, Y., Noda, H., Sasaki, S., Goossens, S., Iwata, T., 2012. Lunar global digital terrain model dataset produced from SELENE (Kaguya) terrain camera stereo observations. In: Proceedings, Lunar and Planetary Science Conference. Woodlands, TX, March 19–23. In: LPS, vol. XLIII, p. 1200.
- Jaw, J.-J., 2000. Control surface in aerial triangulation. *Int. Arch. Photogramm. Remote Sens.* XXXIII (B3), 444–451.
- Kamalakar, J.A., Bhaskar, K.V.S., Laxmi Prasad, A.S., Selvaraj, P., Venkateswaran Kalyanim, R.K., Goswami, A., Sripathi Raja, V.L.N., 2009. Lunar laser ranging instrument (LLRI) a tool for the study of topography and gravitational field of the moon. *Curr. Sci.* 96 (4), 512–516.
- Kato, M., Sasakia, S., Tanaka, K., Iijima, Y., Takizawa, Y., 2008. The Japanese lunar mission SELENE: Science goals and present status. *Adv. Space Res.* 42 (2), 294–300.
- King, B., Guo, J., Chen, Y.Q., Zhang, J.X., Zhang, Y.H., Ning, X.G., 2009. The lunar DEM generation process based on Clementine and Chang'E-1 images. In: Proceedings, International Conference on Geo-spatial Solutions for Emergency Management. Beijing, China, September 14–16.
- Li, C.L., Liu, J.J., Ren, X., Mou, L., Zou, Y., Zhang, H., Lv, C., Liu, J., Zuo, W., Su, Y., Wen, W., Bian, W., Zhao, B., Yang, J., Zou, X., Wang, M., Xu, C., Kong, D., Wang, X., Wang, F., Geng, L., Zhang, Z., Zheng, L., Zhu, X., Li, J., Ouyang, Z., 2010a. The global image of the moon by the Chang'E-1: Data processing and lunar cartography. *Sci. China Earth Sci.* 40 (3), 294–306.
- Li, C.L., Ren, X., Liu, J., Zou, X., Mou, L., Wang, J., Shu, R., Zou, Y., Zhang, H., Lv, C., Liu, J., Zuo, W., Su, Y., Wen, W., Bian, W., Wang, M., Xu, C., Kong, D., Wang, X., Wang, F., Geng, L., Zhang, Z., Zheng, L., Zhu, X., Li, J., 2010b. Laser altimetry data of Chang'E-1 and the global lunar DEM model. *Sci. China Earth Sci.* 40 (3), 281–293.
- Light, D.L., 1972. Altimeter observations as orbital constraints. *Photogramm. Eng.* 38 (4), 339–346.
- Liu, J.J., Ren, X., Mu, L., Zhao, B., Xiang, B., Yang, J., Zou, Y., Zhang, H., Lu, C., Liu, J., Zuo, W., Su, Y., Wen, W., Bian, W., Zou, X., Li, C.L., 2009. Automatic DEM generation from Chang'E-1's CCD stereo camera images. In: Proceedings 40th Lunar and Planetary Science Conference. Houston, TX, March 23–27, p. 2570.
- Mazarico, E., Rowlands, D.D., Neumann, G.A., Smith, D.E., Torrence, M.H., Lemoine, F.G., Zuber, M.T., 2011. Orbit determination of the lunar reconnaissance orbiter. *J. Geod.* 86, 193–207.
- Ouyang, Z.Y., Li, C., Zou, Y., Zhang, H., Lv, C., Liu, J., Liu, J., Zuo, W., Su, Y., Wen, W., 2010. Preliminary scientific results of Chang'E-1 lunar orbiter. *Sci. China* 53 (11), 1565–1581.
- Radhadevi, P.V., Solanki, S.S., Nagasubramanian, V., Sudheer Reddy, D., Krishna Sumanth, T., Saibaba, J., Varadarajan, Geeta, 2013. An algorithm for geometric correction of full pass TMC imagery of Chandrayaan-1. *Planet. Space Sci.* 79, 45–51. <http://dx.doi.org/10.1016/j.pss.2013.01.012i>.
- Robinson, M.S., Speyerer, E.J., Boyd, A., Waller, D., Wagner, R.V., Burns, K.N., 2012. Exploring the Moon with the lunar reconnaissance orbiter camera. *Int. Arch. Photogramm. Remote Sens. Spat. Inf. Sci.* XXXIX-B4, 501–504.
- Rosiek, M., Kirk, R., Hare, T., Howington-Kraus, E., 2001. Combining lunar photogrammetric topographic data with Clementine LIDAR data. In: Proceedings, ISPRS WG IV/9: Extraterrestrial Mapping Workshop "Planetary Mapping 2001". Flagstaff, AZ, October 14–15.
- Scholten, F., Oberst, J., Matz, K.-D., Roatsch, T., Wählisch, M., Speyerer, E.J., Robinson, M.S., 2012. GLD100: The near-global lunar 100 m raster DTM from LROC WAC stereo image data. *J. Geophys. Res., Planets* 117, E00H17.
- Smith, D.E., Zuber, M.T., Neumann, G.A., Lemoine, F.G., 1997. Topography of the Moon from the Clementine LIDAR. *J. Geophys. Res., Planets* 102 (E1), 1591–1611.
- Smith, D.E., Zuber, M.T., Jackson, G.B., Cavanaugh, J.F., Neumann, G.A., Riris, H., Sun, X., Zellar, R.S., Coltharp, C., Connelly, J., Katz, R.B., Kleyner, I., Liiva, P., Matuszeski, A., Mazarico, E.M., McGarry, J.F., Novo-Gradac, A., Ott, M.N., Peters, C., Ramos-Izquierdo, L.A., Ramsey, L., Rowlands, D.D., Schmidt, S., Scott, V.S., Shaw, G.B., Smith, J.C., Swinski, J., Torrence, M.H., Unger, G., Yu, A.W., Zagwodzki, T.W., 2010. The lunar orbiter laser altimeter investigation on the lunar reconnaissance orbiter mission. *Space Sci. Rev.* 150 (1–4), 209–241.
- Spiegel, M., 2007. Improvement of interior and exterior orientation of the three line camera HRSC with a simultaneous adjustment. *Int. Arch. Photogramm. Remote Sens. Spat. Inf. Sci.* 36 (3/W49B), 161–166.
- Teo, T.A., Chen, L.C., Liu, C.L., Tung, Y.C., Wu, W.Y., 2010. DEM-aided block adjustment for satellite images with weak convergence geometry. *IEEE Trans. Geosci. Remote Sens.* 48 (4), 1907–1918.
- Tran, T., Rosiek, M., Ross, R., Beyer, A., Mattson, S., Howington-Kraus, E., Robinson, M.S., Archinal, B.A., Edmundson, K., Harbour, D., Anderson, E., the LROC Science Team, 2010. Generating digital terrain models using LROC NAC images. In: Proceedings, ASPRS/CaGIS 2010 Fall Specialty Conference. Orlando, Florida, November 15–19.
- Vighnesam, N.V., Sonney, A., Gopinath, N.S., 2010. India's first lunar mission Chandrayaan-1 initial phase orbit determination. *Acta Astronaut.* 67 (7–8), 784–792.
- Vondrak, R., Keller, J., Chin, G., Garvin, J., 2010. Lunar Reconnaissance Orbiter (LRO): observations for lunar exploration and science. *Space Sci. Rev.* 150, 7–22.
- Wang, Z.Z., 1990. Principles of Photogrammetry [with Remote Sensing]. Press of Wuhan Technical University of Surveying and Mapping, Publishing House of Surveying and Mapping, Beijing.
- Wang, X.Q., Cui, J., Wang, X.D., Liu, J.J., Zhang, H.B., Zuo, W., Su, Y., Wen, W.B., Rème, H., Dandouras, I., Aoustinb, C., Wang, M., Tan, X., Shen, J., Wang, F., Fu, Q., Li, C.L., Ouyang, Z.Y., 2012. The solar wind interactions with lunar magnetic anomalies: A case study of the Chang'E-2 plasma data near the Serenitatis antipode. *Adv. Space Res.* 50 (12), 1600–1606.
- Wieczorek, M.A., Jolliff, B.L., Khan, A., Pritchard, M.E., Weiss, B.P., Williams, J.G., Hood, L.L., Righter, K., Neal, C.R., Shearer, C.K., McCallum, I.S., Tompkins, S., Hawke, B.R., Peterson, C., Gillis, J.J., Bussey, B., 2006. The constitution and structure of the lunar interior. *Rev. Mineral. Geochem.* 60, 221–364.
- Wu, B., Guo, J., Zhang, Y., King, B., Li, Z., Chen, Y., 2011a. Integration of Chang'E-1 imagery and laser altimeter data for precision lunar topographic modeling. *IEEE Trans. Geosci. Remote Sens.* 49 (12), 4889–4903.
- Wu, B., Zhang, Y., Zhu, Q., 2011b. A triangulation-based hierarchical image matching method for wide-baseline images. *Photogramm. Eng. Remote Sens.* 77 (7), 695–708.
- Wu, B., Zhang, Y., Zhu, Q., 2012. Integrated point and edge matching on poor textural images constrained by self-adaptive triangulations. *ISPRS J. Photogramm. Remote Sens.* 68, 40–55.
- Wu, B., Guo, J., Hu, H., Li, Z., Chen, Y., 2013. Co-registration of lunar topographic models derived from Chang'E-1, SELENE, and LRO laser altimeter data based on a Novel surface matching method. *Earth Planet. Sci. Lett.* 364, 68–84.
- Yoon, J.-S., Shan, J., 2005. Combined adjustment of MOC stereo imagery and MOLA altimetry data. *Photogramm. Eng. Remote Sens.* 71 (10), 1179–1186.
- Zhao, B., Yang, J., Wen, D., 2011. Chang'E-2 satellite CCD stereo camera design and verification. *Spacecraft Eng.* 20 (1), 14–21.
- Zhou, W., Yang, W., 2010. Orbit design for Chang'E-2 lunar orbiter. *Spacecraft Eng.* 19 (5), 24–28.
- Zhu, Q., Wu, B., Wan, N., 2007a. A filtering strategy for interest point detecting to improve repeatability and information content. *Photogramm. Eng. Remote Sens.* 73 (5), 547–553.
- Zhu, Q., Wu, B., Wan, N., 2007b. A subpixel location method for interest points by means of the Harris interest strength. *Photogramm. Rec.* 22 (120), 321–335.
- Zou, X.D., Liu, J.J., Mou, L.L., Ren, X., Li, K., Zhao, J.J., Liu, Y.X., Li, C.L., 2012. Topographic analysis of the proposed landing area of Sinus Iridum. In: EPSC Abstracts, vol. 7. EPSC2012-151-1.